Supplemental Data

Establishing New Sites of Polarization by Microtubules

Nicolas Minc, Scott V. Bratman, Roshni Basu, and Fred Chang

Supplemental Discussion:

a- Bending ratio and MT catastrophe location in bent cells

A simple model based upon geometrical considerations can predict sites of MT contact in a given bent cell. In this description, we define the *bending ratio*, $\gamma = \ell / L$, where L is the cell length and ℓ is twice the distance from the center of the nucleus to the cell cortex along the axis perpendicular to the short axis of the cell (Figure 2C and S2A). This dimensionless parameter represents the change in the distance between the nucleus and the cortex upon cell bending. The bending ratio is 1 in a straight cell, and decreases as a cell becomes more bent (Figure S2B). Given that a MT grows straight from the nucleus to the cortex along the axis perpendicular to the short axis of the cell, we can predict that the MT contacts the cortex at an absolute position of $S_{contact} \approx 1-\gamma$ away from the tip. This value increases as the cell is more bent, indicating that MTs contact the cortex closer to the nucleus as cells become more bent (Figure 2C). In our experimental data, the average location of catastrophes that occurred on the cell side followed a similar trend ($S_{cat}=0.72-0.60\gamma$, Figure 2E). This correlation suggested that contact with the cortex imposed by the bent shape had a critical effect on inducing catastrophe. This trend was independent of cell length, suggesting that global reorganization of MTs upon cell bending was not the result of a length scale inherited from the previous straight cell conformation. Instead, MT reorganization following cell bending, appears to be a consequence of the catastrophes occurring on the cell side. Further, because the cell side is closer to the nucleus in the bent cell (by a factor γ), MTs are notably shorter on average than they are in a straight cell of same length.

b-Hot spots analysis of catastrophe

To test whether hot spots distributions were significantly different from a random distribution, we compared these experimental data with a large set of Monte Carlo simulations. For each cell we measured the length Lc corresponding to the cortex stretch where the n catastrophes occurred (in a typical bent cell, this excludes most of the zone around the nucleus and part of the tips) and the spatial resolution, r, at which we could detect a catastrophe event. These define a number of sites N=[Lc/r], where catastrophes could possibly occur. The Monte-Carlo trials generated 1000 random distributions of the n catastrophes in these N sites and returned a vector [k_1 k_2 k_3…], where k_i is the number of clusters of i catastrophes ($n = \sum ik_i$). The multinomial probability associated with the Monte-Carlo vector and with the experimental data were computed as :

$P_{multi} = \frac{n!}{N^n \prod ((i)!)^{k_i}}$. The probability, *p*, of obtaining the experimental distribution as compared to a randomized trial is thus obtained by: $p = \frac{P_{multi}(Experimental)}{P_{multi}(Montecarlo)}$. This analysis showed that these experimental distributions are significantly different from those arising by chance. Typically, the probability of a given distribution of hot spots was 100-10000 times smaller than a distribution arising from a random clustering of events generated by the simulation (see values of *p* in bar plots of Figure 2E and S4A). The value of p allows to undoubtedly discern a non-random from a random distribution when smaller than 0.01.

c- Relationships between cortex curvature and sites of MT catastrophe and bud6p recruitment.

Sites of MT catastrophe in bent cells were not obviously due to cell surface perturbations from the bending. Catastrophe sites did not correspond to areas of maximum curvature; many sites were located at relatively “unbent” parts of the cell (Figure 2E). The location of catastrophe on the cell side was independent of cell curvature (Figure S6A). Importantly, in a subset of cells that popped out of the well into their original straight conformation, MTs rearranged almost immediately along the long axis of the cell, illustrating the rapid response of the MT cytoskeleton organization to a given cell shape

(Figure S5A and Movie 4). Further, preliminary results suggest that similar hot spot distributions can also be found at the tips of normal non-bent cells (our unpublished data). The regions of bud6p accumulation also did not correlate with sites of maximal curvature, and sometimes occurred in cortical regions that were not curved (Figure 3B, 4A). The location of bud6-3GFP on the cell side was independent of cell curvature (Figure S6B). Further, in cells that were bent only transiently (for about 1-2 minutes), but then popped out of the well and straightened back into a rod shape, no bud6p redistribution was apparent (Figure S5B).

SUPPLEMENTARY FIGURE LEGENDS

Figure S1. PDMS array of microchambers with varying sizes.

The picture at the center represents the PDMS replica onto which cells are placed. This replica encompasses 8 regions, each composed of 2500 cylindrical microchambers with varying diameters (from 10 to 50µm). The three other pictures depict examples of these different regions (black=10µm, red=25µm, blue=50µm holes) covered with yeast cells. Scale bar: 20µm.

Figure S2. Growth rates of bent cells and methods for generating different bent cells.

(A) Schematic representing the important geometrical parameters for computing the bending ratio of a cell in a round chamber. L_0 is the diameter of the well, L the cell length, and d the cell diameter. R is the radius of curvature of the bent cell and ℓ is twice the distance from the center of the nucleus to the side of the cell following the axis perpendicular to the short axis of the cell. The bending ratio, $\gamma = \ell /L$, thus describes how close the cortex is from the nucleus along the former axis of the cell. For a straight cell $\gamma = 1$ and for a bent cell : $\gamma = \frac{1}{L}\sqrt{4Rd - d^2}$. The radius of curvature R of a given cell bent in a given hole can be computed and follows: $L_0 = 2R\sin(\frac{L}{2R})$ for $L \le \frac{\pi L_0}{2}$ and $R = \frac{L_0}{2}$ for $L \ge \frac{\pi L_0}{2}$ .These equations can be computationally inverted to finally compute and plot γ as a function of L for different values of L_0 as depicted in C. (B) Pictures of wild-type cells of varying length, bent in holes of different sizes. Values in yellow correspond to the bending ratio, γ, and in white to the cell length, L. Strain: FC504. (C) Mathematical representation of the bending ratio, γ, as a function of cell length for different well sizes. In theses plots, the superimposed dots correspond to the cells depicted in B. Scale bars: 10µm. (D) Time lapse of a cell initially bent which grows and goes through an entire cell cycle in a microchamber. Values of actual elongation rates measured for straight and bent cells growing inside microchambers (n=10 for each condition). The error bars represent the standard deviation. Strain: FC504 (*cdc25-22* at 25°C). Scale bar: 5µm

Figure S3. Interphase MT behavior in bent cells.

(A) Time-lapse imaging of a cell expressing GFP-tubulin bent in a 25μm chamber. MT bundles track the outer curvature of the cell, often bending significantly without breaking. One example is marked by purple arrowheads. This MT grows in constant contact with the cortex until it undergoes catastrophe (yellow arrowheads) and shrinks away (white arrowhead). Images are maximum projections of confocal stacks. Time is in min:sec. Strain: NM11 (*cdc25-22* at 25°C). (B) Quantification of interphase MT plus end behavior in the cytoplasm. Cells expressing GFP-tubulin were placed into microchambers, and rates of plus end growth and shrinkage were determined from time-lapse maximum projection confocal images (n=20 for each parameter). Growing MTs were examined prior to coming in contact with cortex. There were no statistically significant differences in these measurements, indicating that bending of the cells does not noticeably perturb MT plus end dynamics within the cytoplasm. (Bottom) Same measurement for straight cells with different lengths. The error bars represent the standard deviation. Strain: NM11. (C) Plus end growth rate at the cell cortex as a function of the average angle of MT-cortical contact. Growth rates were determined for the entire MT prior to buckling or catastrophe using single focal plane time-lapse imaging and fluorescent speckle analysis. Error bars represent experimental uncertainties. Strain NM11.

Figure S4. Hot spots distributions and significance at the side of bent cells.

(A) Schematic of MT catastrophe events in bent cells. MT catastrophes were determined from time-lapse images of GFP-tubulin. Specific points on the cortex that experience multiple catastrophe events are indicated (orange and red dots) and further represented in the corresponding bar plot on the right. Dots size and bar width encompass the error made in the measurement. Numbers on the top right of each bar plot represents the probability of having this particular distribution as compared to a random trial. Strain: NM11 (cdc25-22 at 25°C). Scale bars: 5μm. (B) Hot spots do not arise only by chance. Histogram representing the clustering of catastrophe events in the three cells presented in (A) and in corresponding Monte-Carlo trials (see supplementary text). (C) Time-lapse images corresponding to the second cell in A illustrating the presence of a hot spot

(indicated by the arrow). The number at the bottom counts the number of catastrophes occurring at this site. Strain NM11. Scale bar: 5µm.

Figure S5. Response of MTs and bud6p to transient cell bending.
Cells expressing GFP-tubulin (A) or bud6-3GFP (B) were imaged before and after being pushed into microchambers. Cells buckled into the chambers by over-focusing with the objective (for ~2 minutes). When the objective was refocused, the cells quickly straightened and popped out of the chambers. This transient cell bending did not change the distribution of MTs or bud6p in straight cells. Maximum projection confocal images are shown. Strains: NM11 and NM01 (*cdc25-22* at 25°C). Scale bars: 5µm.

Figure S6. Role of curvature in MT catastrophe/ bud6p redistribution.
(A) The average absolute position of catastrophe events on the cell side is independent of the radius of curvature (Correlation coefficient: 0.21). (D) The absolute position of bud6p on the cell side in independent of the radius of curvature (Correlation coefficient: -0.15).

Figure S7 Ectopic recruitment of tea1p in bent cells.
(A) Tea1-3GFP localization in straight and bent cells. Strain: RB03 (*cdc25-22* at 25°C). (B) Tea1p localizes predominantly at MT plus ends in contact with the cell sides. Strain: NM39. Scale bars: 5µm.

Figure S8. Distribution of for3p in *tea1*Δ, *moe1*Δ and *mal3*Δ bent cells .
(A) For3-3GFP localization in straight and bent *tea1*Δ, *moe1*Δ and *mal3*Δ cells in the presence and the absence of LatA. (B) Proportion of bent cells that show a specific localization of for3-3GFP to the cell side in the indicated genetic backgrounds and conditions (n≈30 for each condition). Strains: NM09, NM07, NM70 + HU and RB112 + HU. Scale bar: 5µm.

Figure S9. Distribution of bud6p in bent cells.

Bud6-3GFP position in a normal and bent cell of the indicated mutants. Strains: NM32, NM49 + HU, NM44 + HU, NM50 + HU, NM47 + HU, NM45 + HU, NM46 + HU. Scale bars: 5µm. * For this experiment, the temperature of the objective was raised to 30°C with a Bioptechs objective heater.

Figure S10. Interphase MT behavior in *mal3*Δ and *moe1*Δ straight and bent cells.
(A) Catastrophe mapping in bent *mal3*Δ and *moe1*Δ cells and the corresponding merged image over 10 minutes. Strains: SB408 + HU, RB65 + HU. (B) Quantification of interphase MT plus end behavior in the cytoplasm of *mal3*Δ and *moe1*Δ cells. Cells expressing GFP-tubulin were placed into microchambers, and rates of plus end growth and shrinkage were determined from time-lapse maximum projection confocal images (n is indicated for each parameter).

Figure S11. A new pathway involving mal3p, moe1p and for3p responsible for linking polarity by MTs is parallel to the tea1p-tea4p pathway.
(A) Co-immunoprecipitation of endogenously expressed moe1-GFP and for3-myc from yeast extracts. To prepare yeast extracts, cells were grown in minimal media, harvested, washed and resuspended in an equal volume of CXS buffer (50mM Hepes, pH 7.5, 20 mM KCl, 1mM $MgCl_2$, 2mM EDTA, and protease inhibitor cocktail). The slurry was frozen as pellets in liquid nitrogen and ground into a powder. 3 ml of the resulting powder was thawed and protease inhibitors were added. The slurry was centrifuged at 13.2krpm for 10 mins at 4^{o}C. 0.1% Triton X-100 was added to the supernatant and was centrifuged at 45krpm for 30 min at 4^{o}C to obtain the soluble yeast extract. For immunoprecipitation, Dynal sheep anti-mouse beads were washed twice in PBS, and preincubated for 2 hours with 0.8µg monoclonal anti-GFP antibody (Roche) and 1mg/mL BSA (Sigma). The beads were then washed and incubated with 100µL of soluble yeast extract for 2 hours at 4^{o}C. After incubation, beads were washed extensively, boiled in 50µL of 1X sample buffer and loaded onto 6% SDS-PAGE gels. For immunoblotting monoclonal anti-GFP antibody (Roche) and polyclonal anti-myc antibody A-14 (Santa Cruz Biotechnology) were used. Co-immunoprecipitation was observed in three independent experiments. (B) Polarity and cell shape of wildtype, *mal3*Δ, *moe1*Δ, *tea1*Δ,

*tea1*Δ *mal3*Δ and *tea1*Δ *moe1*Δ in the indicated conditions. Error bars represent standard variations arising from different experiments. Number of cells for each point, n ≈ 100. Strains: FC420, FC1440, RB75, NM68 and NM72.

Table S1. *S. pombe* strains used in this study.

NM01	cdc25-22 bud6-3GFP:kanMX
NM07	cdc25-22 for3-3GFP:ura4+
NM09	cdc25-22 tea1Δ::ura4+ for3-3GFP:ura4+
NM11	cdc25-22 sv40:GFP-atb2 [leu1+]
NM14	cdc25-22 tea1Δ::ura4+ bud6-3GFP:kanMX
NM15	cdc25-22 leu1-::GFP-bgs4:leu1+
NM19	cdc25-22 bud6-3GFP:kanMX pSB62[pnmt41:mRFP-atb2; LEU2]
NM20	cdc25-22 tea1Δ::ura4+ sv40:GFP-atb2 [leu1+]
NM24	bud6-3GFP pSB62 [pnmt41:mRFP-atb2; LEU2]
NM30	cdc25-22 tip1Δ::kanMX bud6-3GFP:kanMX
NM32	cdc25-22 mod5Δ::kanMX bud6-3GFP:kanMX
NM33	cdc25-22 leu1-::nmt41:GFP-CHD^{rng2}:leu1+
NM34	cdc25-22 bud6-GFP:kanMX tea4Δ::kanMX
NM39	cdc25-22 tea1-3GFP:kanMX pSB62[pnmt41:mRFP-atb2; LEU2]
NM42	cdc25-22 bud6-tomato:natMX sv40:GFP-atb2 [leu1+]
NM43	cdc25-22 tea3Δ::kanMX
NM44	bud6-3GFP:kanMX tea3Δ::kanMX
NM45	bud6-3GFP:kanMX mto1Δ::natMX
NM46	bud6-3GFP:kanMX cls1-36:ura4+
NM47	bud6-3GFP:kanMX tea2Δ::his3+
NM48	cdc25-22 bud6-3GFP:kanMX mal3Δ::his3+
NM49	bud6-3GFP:kanMX pom1Δ::ura4+
NM50	bud6-3GFP:kanMX tea1Δ::ura4+ tea3Δ::kanMX
NM59	cdc25-22 cdc42-A6-GFP:kanMX
NM68	moe1Δ::ura4+ tea1Δ::ura4+
NM70	mal3Δ::his 3 for3-3GFP:kanMX
NM72	mal3Δ::his 3+ tea1Δ::natMX
NM117	cdc25-22 bud6-3GFP:kanMX moe1Δ::ura4+
NM115	cdc25-22 bud6-3GFP:kanMX for3Δ::kanMX
NM145	cdc25-22 CRIG-GFP:ura4+
NM151	cdc25-22 moe1Δ::ura4+ tea1Δ::ura4+ bud6-3GFP:kanMX
SB408	mal3Δ::his3+ sv40:GFP-atb2 [leu1+]
RB03	cdc25-22 tea1-3GFP:kanMX
RB65	moe1Δ::ura4+ sv40:GFP-atb2 [leu1+]
RB75	moe1Δ::ura4+
RB112	moe1Δ::ura4+ for3-3GPF:kanMX
RB273	moe1-GFP:kanMX for3-myc:kanMX
FC420	WT
FC504	cdc25-22
FC691	tea1Δ::ura4+
FC1440	mal3Δ::his 3+
FC1451	cdc25-22 cut11-GFP:ura4+ rlc1-GFP:kanMX pDQ105[pnmt1:GFP-atb2; LEU2]

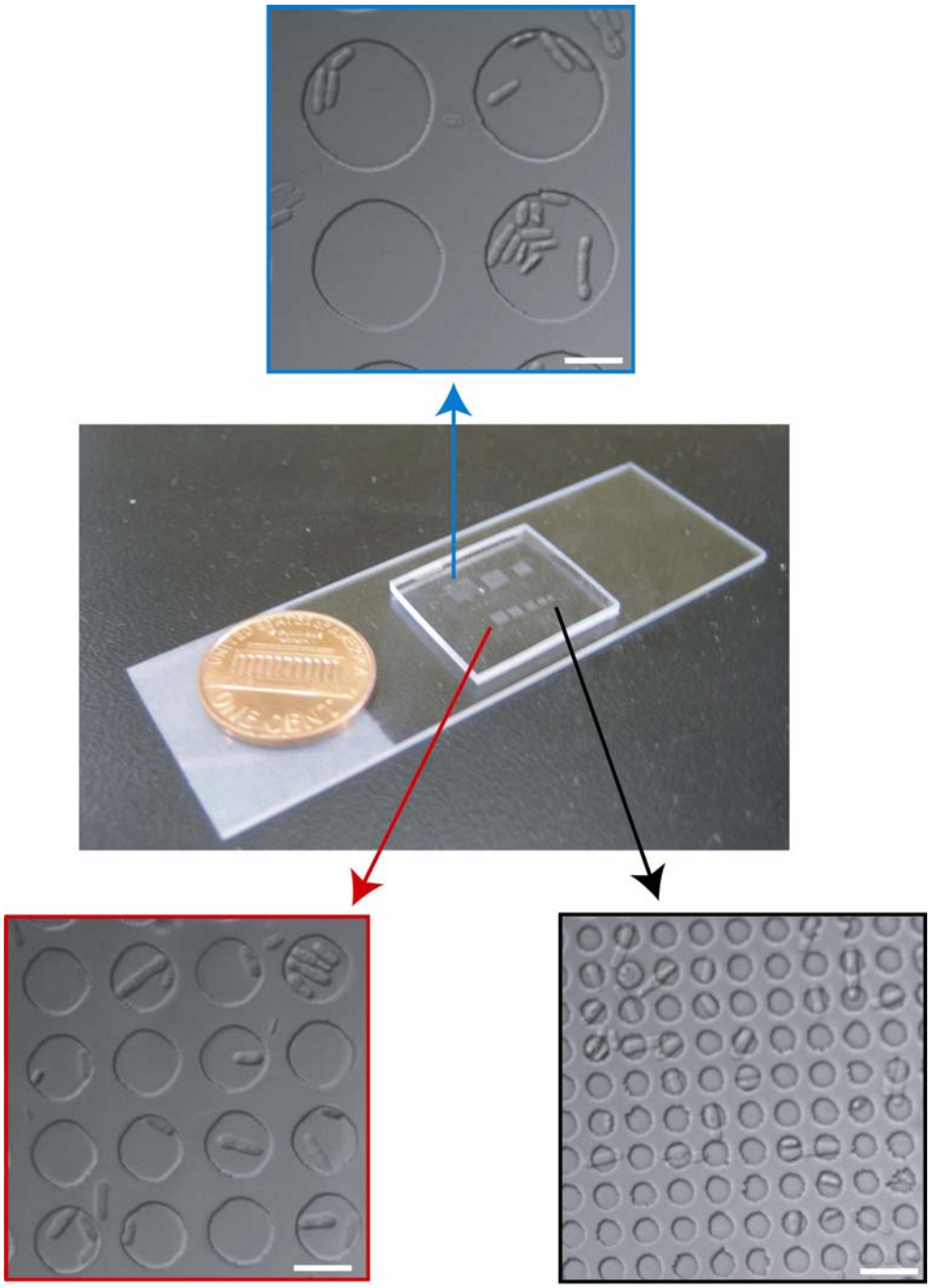

Figure S1

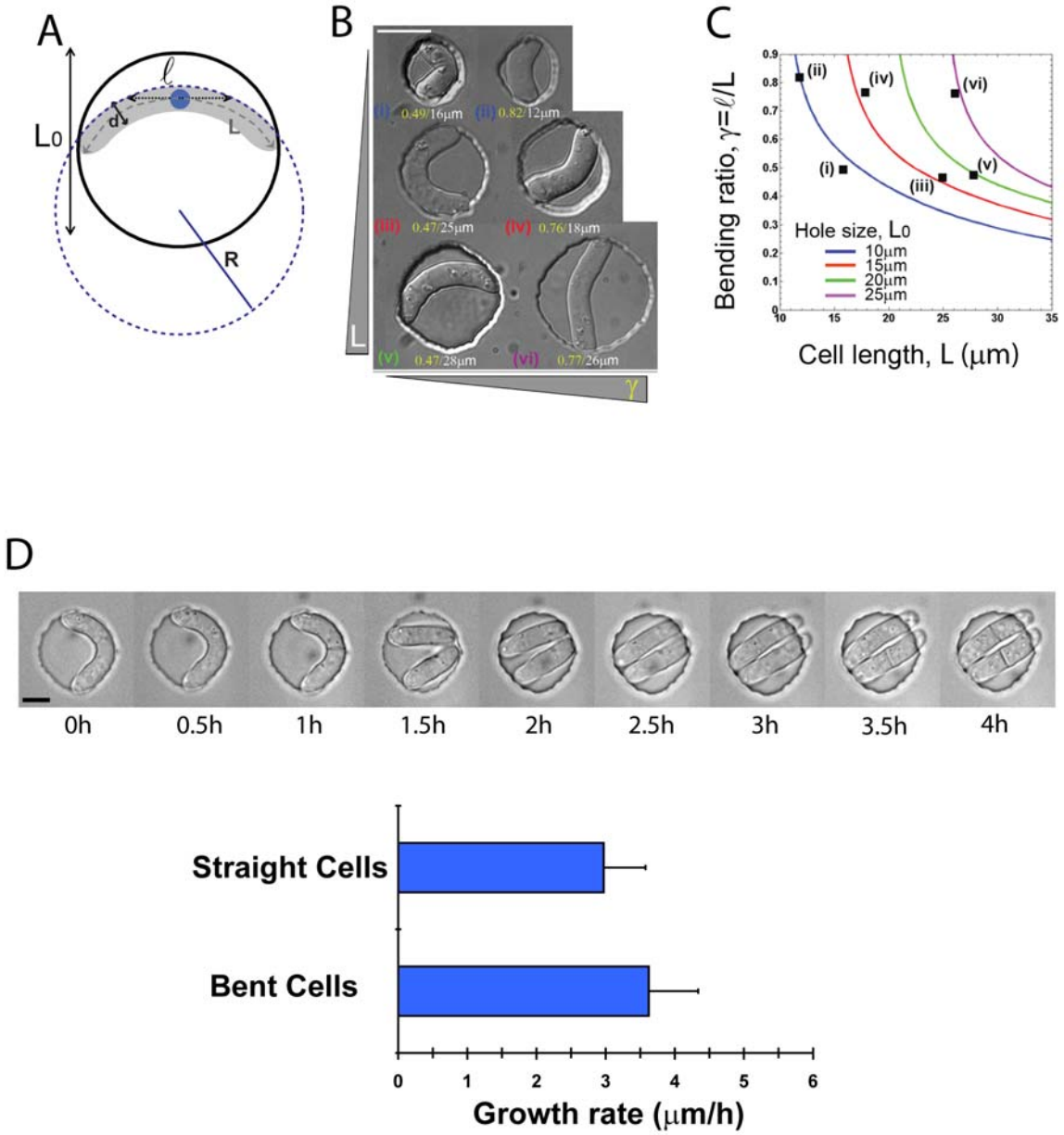
A
B
C
D
L0
R
L
γ
(i) 0.49/16μm
(ii) 0.82/12μm
(iii) 0.47/25μm
(iv) 0.76/18μm
(v) 0.47/28μm
(vi) 0.77/26μm
Bending ratio, γ=ℓ/L
Cell length, L (μm)
Hole size, L0
10μm
15μm
20μm
25μm
0h
0.5h
1h
1.5h
2h
2.5h
3h
3.5h
4h
Straight Cells
Bent Cells
Growth rate (μm/h)

Figure S2

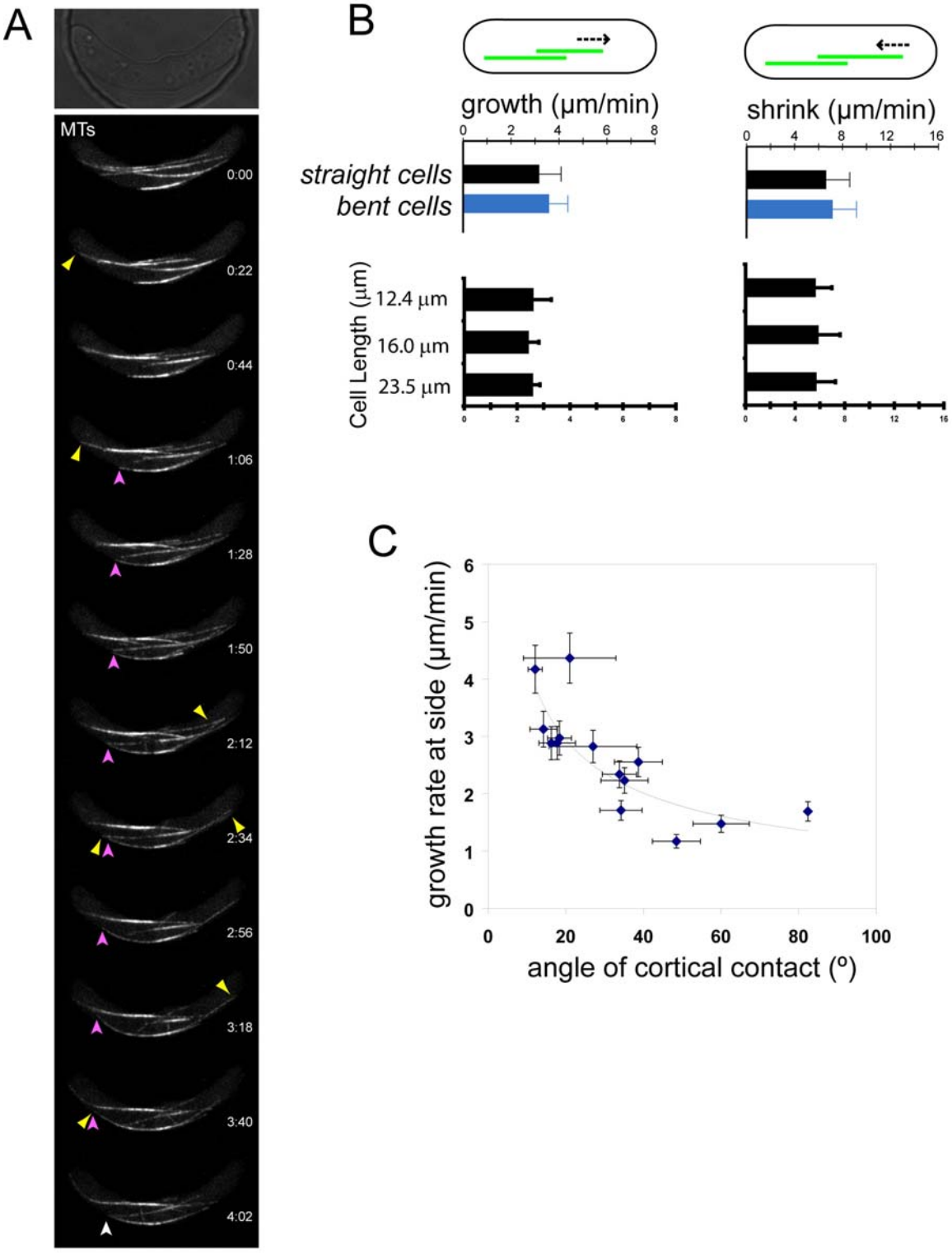
A
MTs
0:00
0:22
0:44
1:06
1:28
1:50
2:12
2:34
2:56
3:18
3:40
4:02
B
growth (μm/min)
shrink (μm/min)
straight cells
bent cells
Cell Length (μm)
12.4 μm
16.0 μm
23.5 μm
C
growth rate at side (μm/min)
angle of cortical contact (º)

Figure S3

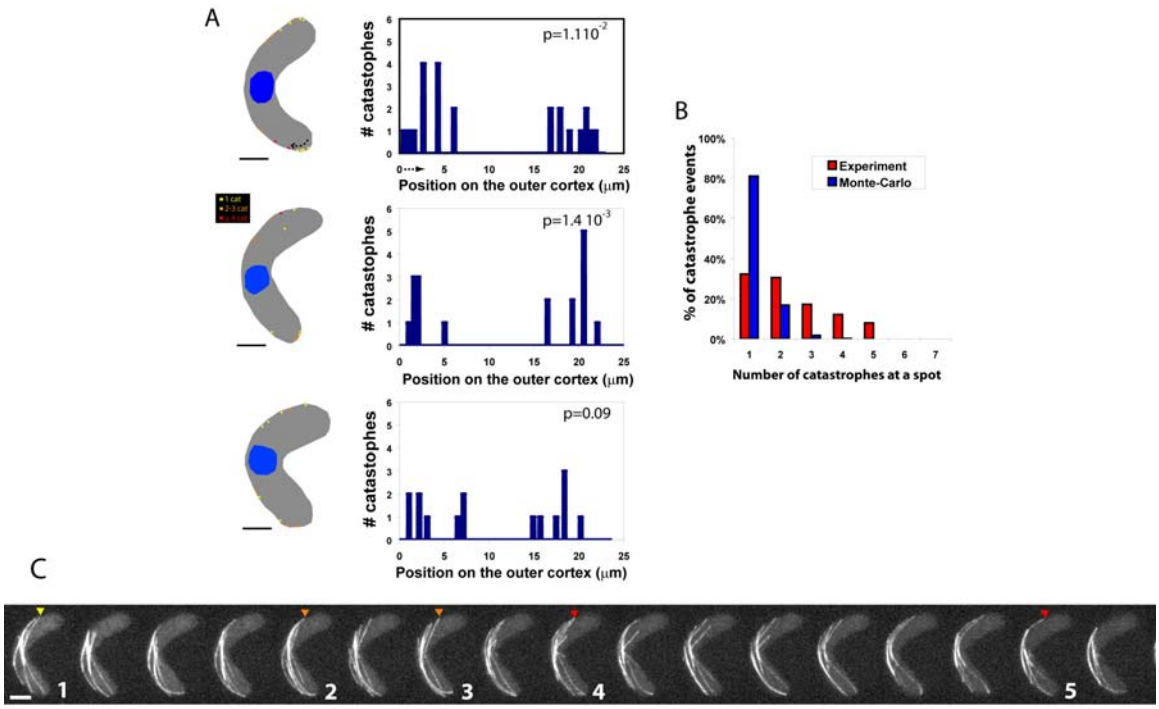
A
# catastophes
p=1.110-2
Position on the outer cortex (μm)
p=1.4 10-3
p=0.09
B
% of catastrophe events
Experiment
Monte-Carlo
Number of catastrophes at a spot
C
1
2
3
4
5

Figure S4

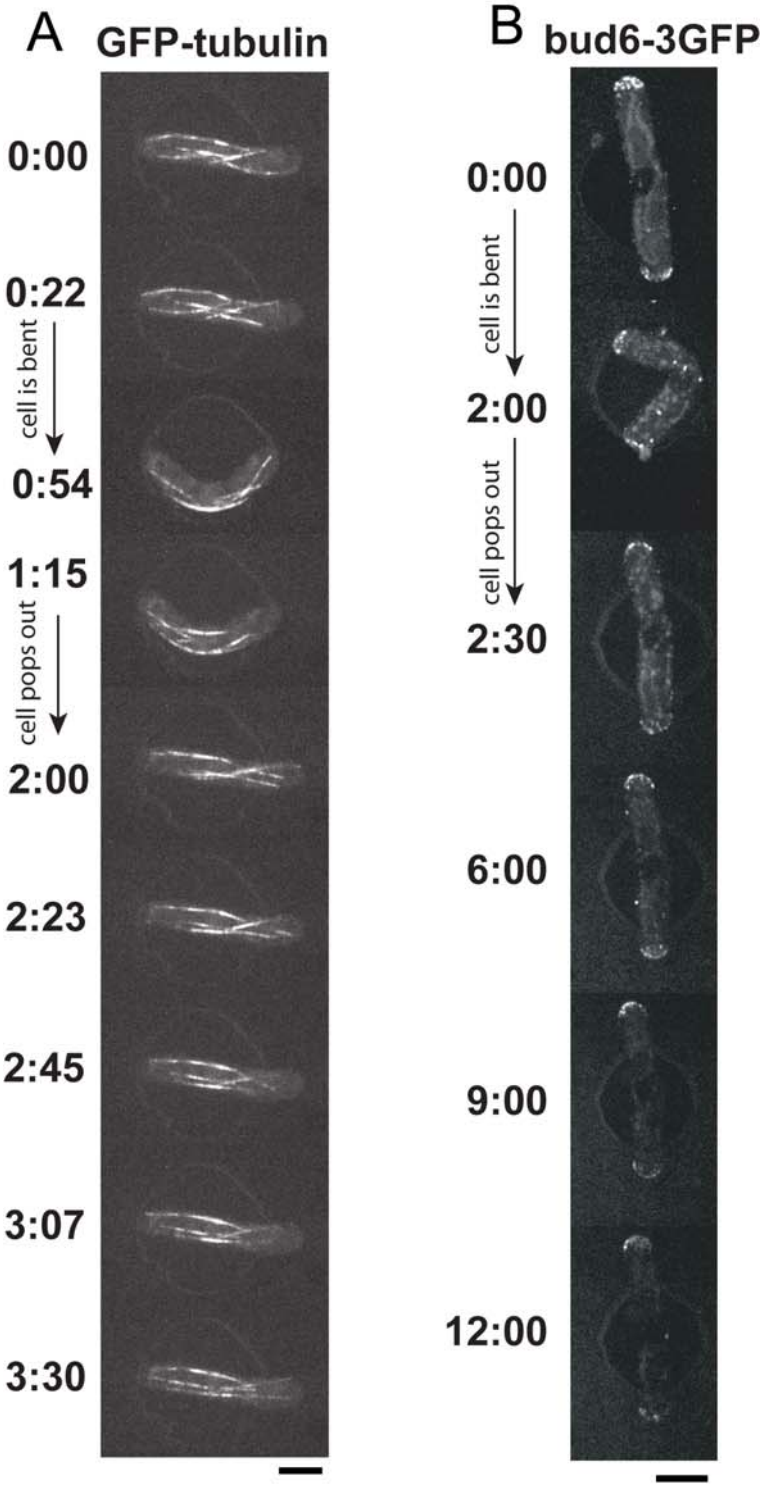
A
GFP-tubulin
0:00
0:22
cell is bent
0:54
1:15
cell pops out
2:00
2:23
2:45
3:07
3:30
B
bud6-3GFP
0:00
cell is bent
2:00
cell pops out
2:30
6:00
9:00
12:00

Figure S5

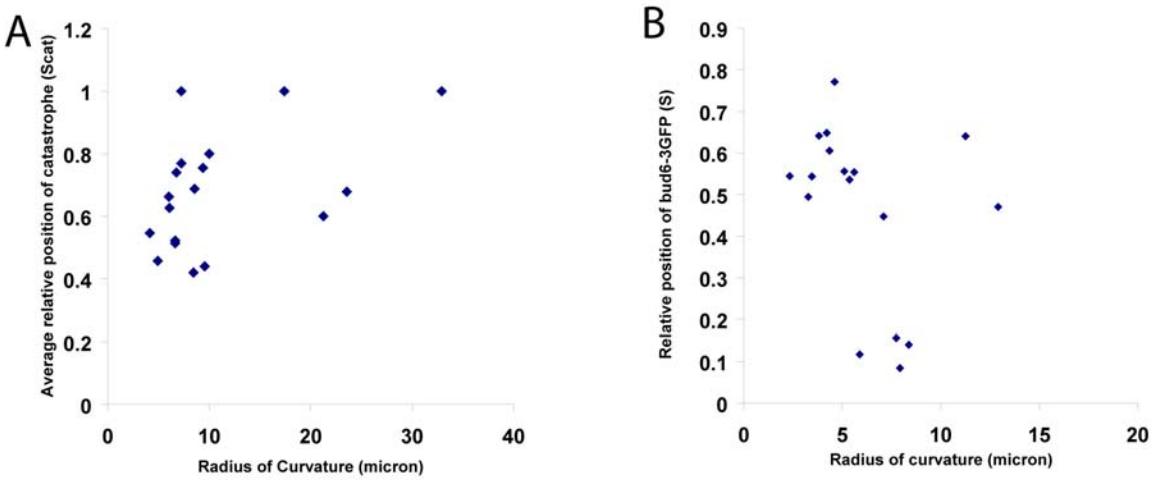
A
Average relative position of catastrophe (Scat)
1.2
1
0.8
0.6
0.4
0.2
0
0
10
20
30
40
Radius of Curvature (micron)
B
Relative position of bud6-3GFP (S)
0.9
0.8
0.7
0.6
0.5
0.4
0.3
0.2
0.1
0
0
5
10
15
20
Radius of curvature (micron)

Figure S6

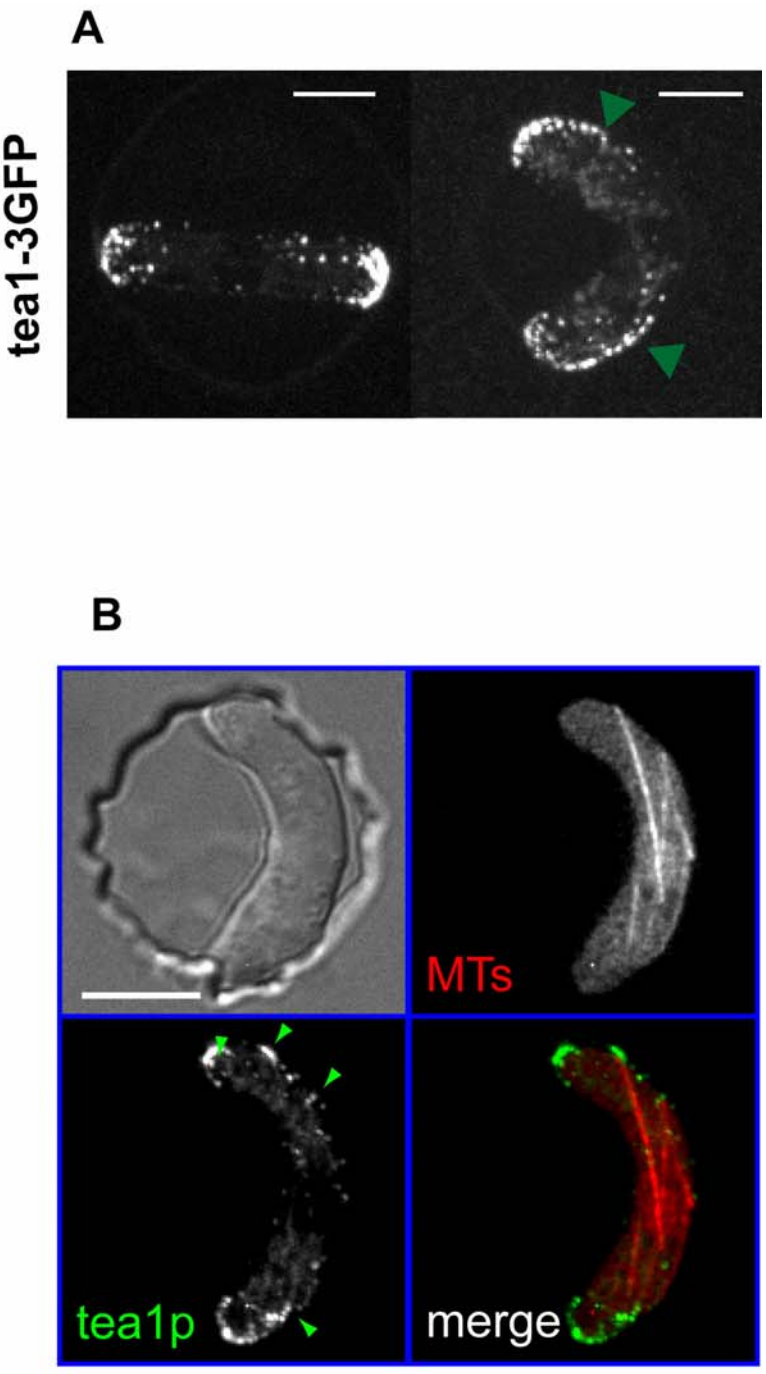

Figure S7

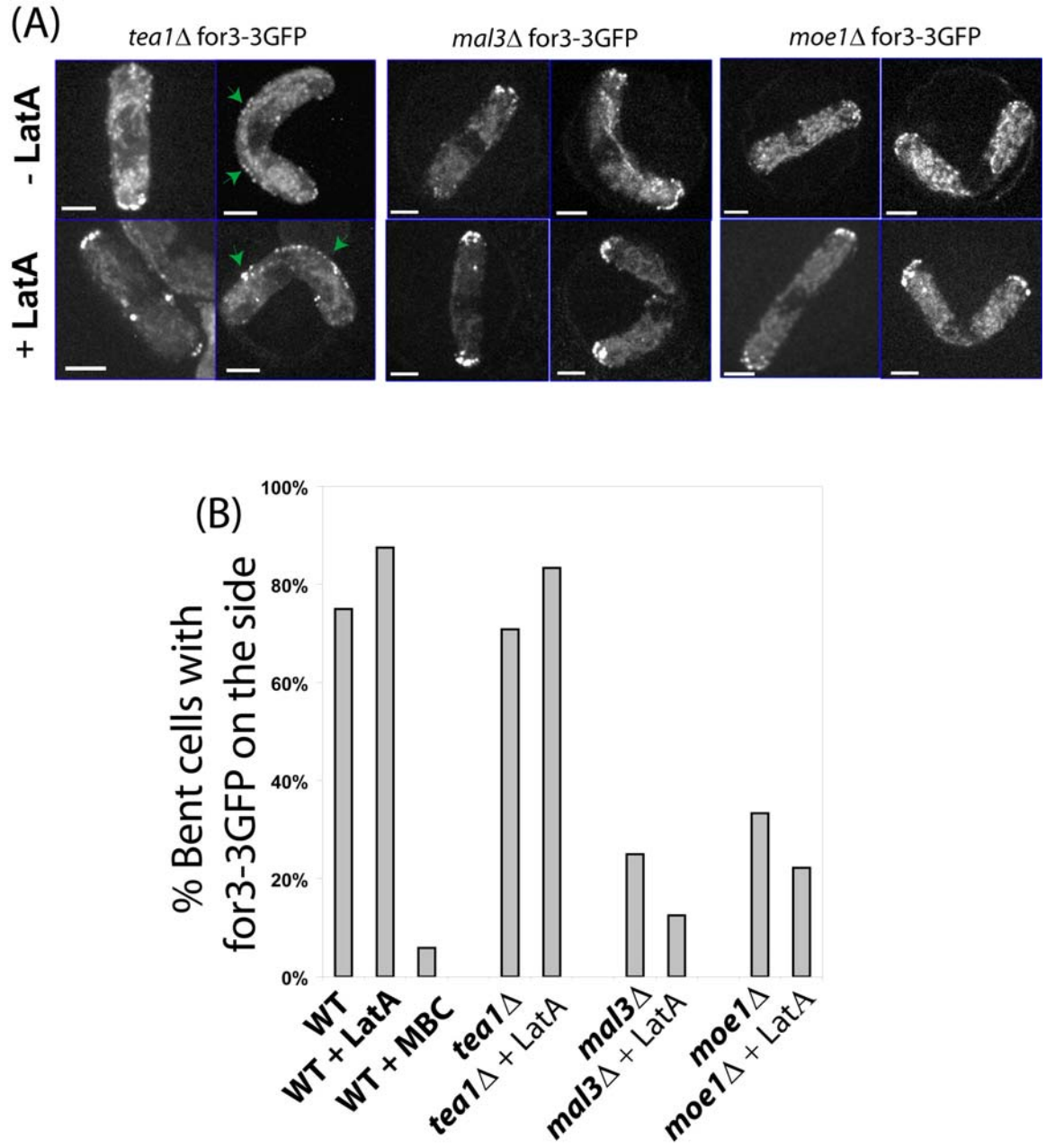
(A)
tea1Δ for3-3GFP
mal3Δ for3-3GFP
moe1Δ for3-3GFP
- LatA
+ LatA
(B)
% Bent cells with for3-3GFP on the side
100%
80%
60%
40%
20%
0%
WT
WT + LatA
WT + MBC
tea1Δ
tea1Δ + LatA
mal3Δ
mal3Δ + LatA
moe1Δ
moe1Δ + LatA

Figure S8

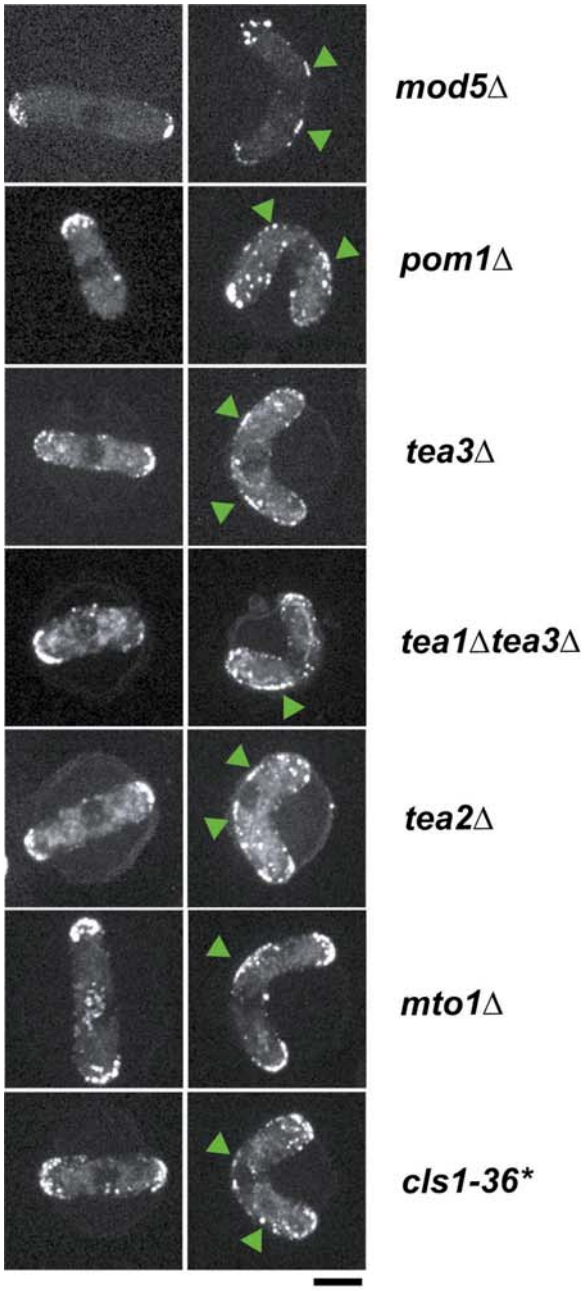

Figure S9

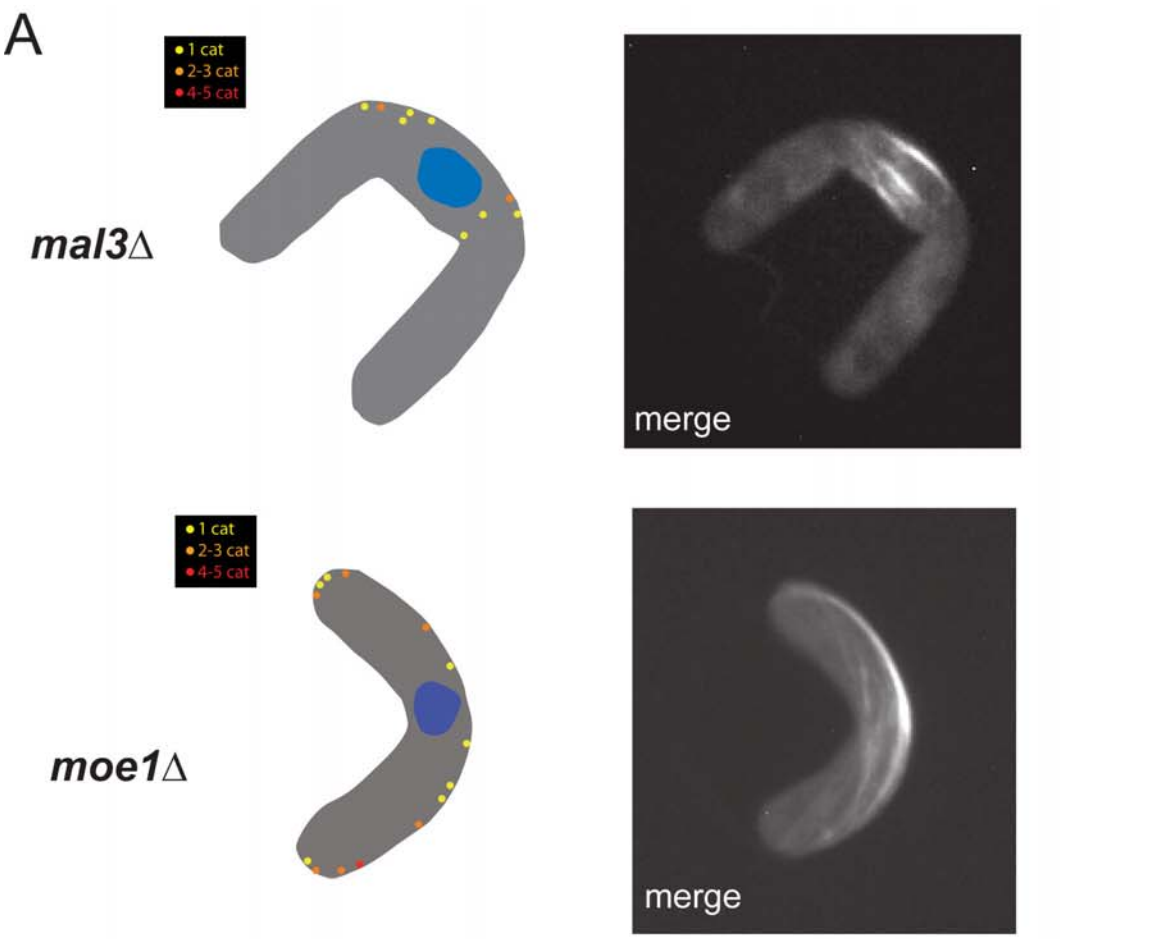
A
1 cat
2-3 cat
4-5 cat
mal3Δ
merge
1 cat
2-3 cat
4-5 cat
moe1Δ
merge

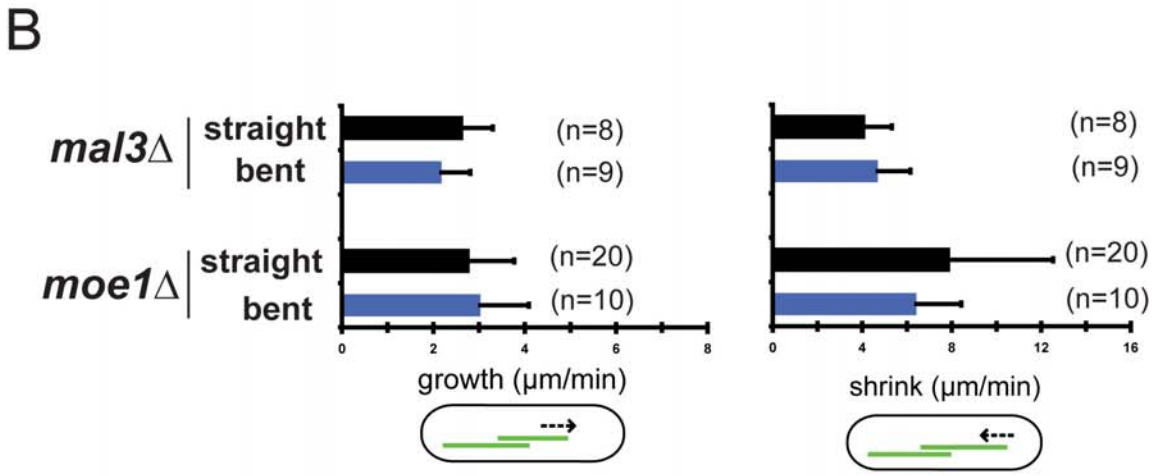
B
mal3Δ
straight
bent
(n=8)
(n=9)
moe1Δ
straight
bent
(n=20)
(n=10)
0
2
4
6
8
growth (μm/min)
(n=8)
(n=9)
(n=20)
(n=10)
0
4
8
12
16
shrink (μm/min)

Figure S10

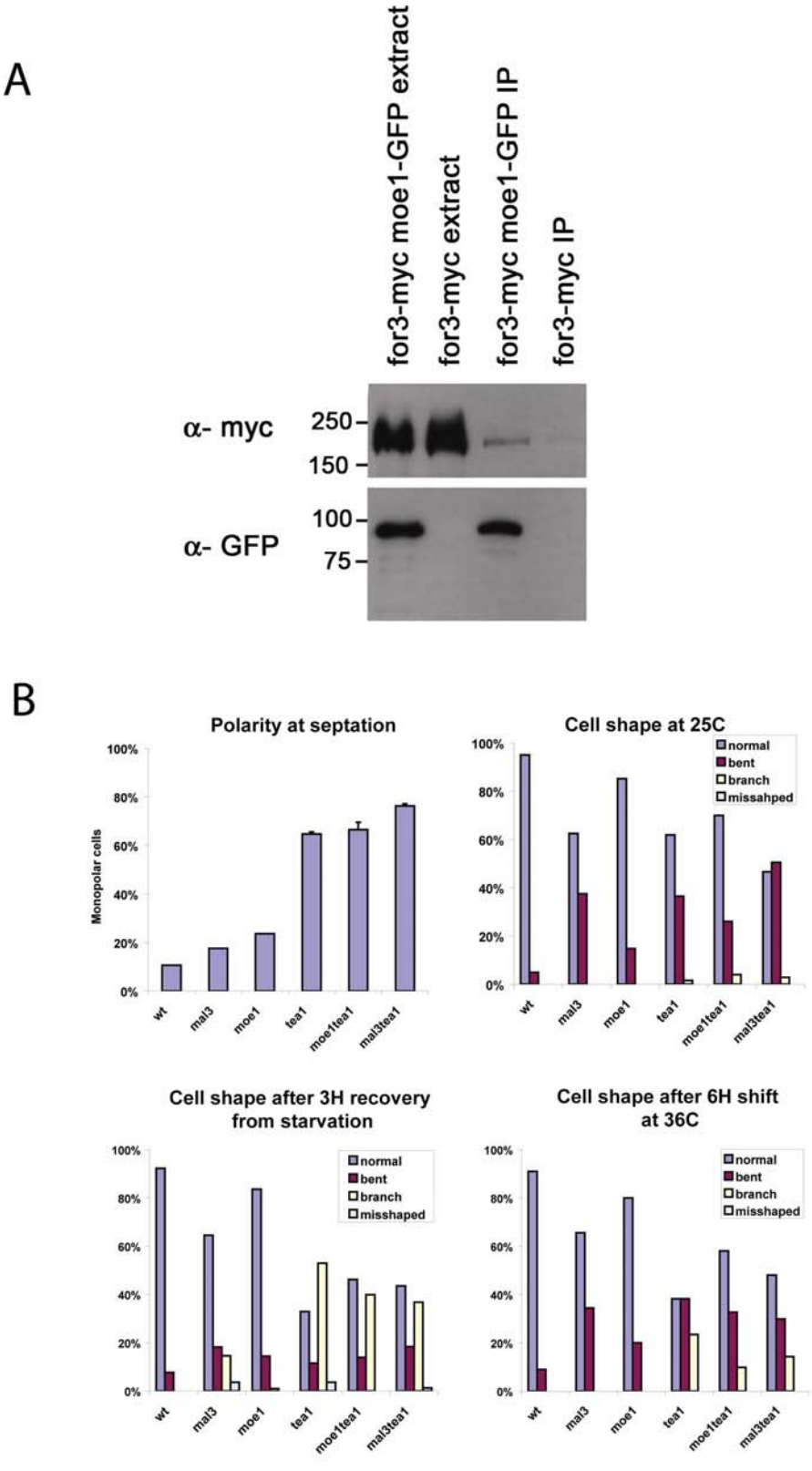
A
for3-myc moe1-GFP extract
for3-myc extract
for3-myc moe1-GFP IP
for3-myc IP
α- myc
250
150
α- GFP
100
75
B
Polarity at septation
Monopolar cells
100%
80%
60%
40%
20%
0%
wt
mal3
moe1
tea1
moe1tea1
mal3tea1
Cell shape at 25C
normal
bent
branch
missahped
Cell shape after 3H recovery from starvation
misshaped
Cell shape after 6H shift at 36C

Figure S11